Wall-modeled LES of a spatially-developing non-equilibrium turbulent boundary layer

By M. Cho, G. I. Park† AND P. Moin

1. Motivation and objectives

Current subgrid-scale (SGS) stress models for large-eddy simulation (LES) are known to produce insufficient turbulent shear stress in the near-wall region of high Reynolds number wall turbulence when the grid is coarse (Jiménez & Moser 2000; Sayadi & Moin 2012). An obvious workaround is to deploy fine enough meshes so that the SGS models perform well close to the wall. This wall-resolved approach however can be prohibitively expensive, because scale separation required for cost economy and accuracy of LES depletes toward the wall. This makes resolution of the energetic motions near the wall as costly as that of the smallest dissipative eddies as required in direct numerical simulation (DNS). Wall-resolved LES of practical high Reynolds number applications is therefore deemed unaffordable, even in the forthcoming exa-scale computing era. Such unfavorable cost scaling of the wall-resolved approach and the need for auxiliary near-wall model to complement the modeled stress were recognized since 1970s (Deardorff 1970; Schumann 1975; Chapman 1979; Choi & Moin 2012). LES conducted with such a wall model is termed wall-modeled LES. It is expected that wall-modeled LES, along with the hybrid approach (Spalart 2009) where the resolved outer solution blends into the Reynolds-averaged near-wall solution, will soon enable predictive and affordable scale-resolving calculations of high Reynolds number wall turbulence (Slotnick *et al.* 2014).

Most wall models are available in the form of wall-stress models. Piomelli (2008) and Larsson *et al.* (2016) provide comprehensive reviews on the traditional wall-stress models, ranging from simple law-of-the-wall type algebraic models to complex partial differential equation (PDE) type models. Bose & Park (2018) discussed recent improvements to the wall-modeling techniques during the last decade, particularly with regard to application of wall-modeled LES to increasingly complex flows (e.g., smooth- and bluff-body separation, transitional boundary layer, shock-boundary layer interaction, high-speed flows) and emergence of the new type of wall models.

The wall-modeled LES techniques have not yet gained much popularity from industry, especially from the external aerodynamics sector where the hybrid methodology remains as a pervasive tool. This is noteworthy, as wall-modeled LES with far reduced empiricism compared to the hybrid approach is potentially better suited to certification by analysis. Convenience in converting existing Reynolds-averaged Navier-Stokes (RANS) solvers to hybrid ones could be a reason that wall-modeled LES has been less favored. A more fundamental criticism of wall-modeled LES, however, is that most studies so far have focused on statistically two-dimensional flows, leaving the performance of wall models in realistic geometries involving three-dimensional turbulent boundary layer (3DTBL) largely unknown. Therefore, it is important to carefully assess the performance of wall

† Department of Mechanical Engineering, University of Pennsylvania

models in 3DTBLs in the presence of strong nonequilibrium effects (e.g., complex pressure gradients, rapid variations in the strain and vorticity).

A 3DTBL is characterized by a skewed mean velocity profile, where direction of the flow changes continually with wall distance. The crossflow velocity can be induced by the lateral wall motion or the spanwise pressure gradient imposed by the wall geometry. Typical examples include the bow and stern regions of ships, swept-back wings, curved ducts, and turbomachinery. A 3DTBL can exhibit several peculiar features that are difficult to model in the prevailing approaches. Turbulent shear stress is often reduced despite the presence of the extra mean rate-of-strain. Unlike in two-dimensional equilibrium boundary layers, the Reynolds shear stress and the mean shear are often misaligned. The Boussinesq approximation with isotropic eddy viscosity adopted in most LES and wall models will be therefore challenged in 3DTBL. Additionally, the widely used equilibrium-type algebraic wall models, which assume that the local wall-stress vector is aligned with the LES velocity at the matching location, can lead to inaccurate predictions.

Recently, Giometto *et al.* (2017) investigated the predictive capabilities of an ordinary differential equation (ODE) equilibrium wall model (Kawai & Larsson 2012), an integral nonequilibrium wall model (Yang *et al.* 2015), and a PDE nonequilibrium wall model (Park & Moin 2014) for a temporally developing 3DTBL in a transient channel flow. Here, mean three dimensionality was generated by imposing a sudden spanwise pressure gradient. Simulation started from a converged statistically two-dimensional flow at $Re_\tau = u_\tau \delta/\nu = 934$, where u_τ is the wall-shear velocity, δ is the channel half-height, and ν is the kinematic viscosity. Accuracy of the wall models during the initial transient where the flow turning rate in the near-wall region peaks was the focus of the study. It was found that the accuracy in terms of the magnitude and direction of the wall stress was proportional to the model complexity: the PDE and the integral models agreeing well with the DNS, whereas the ODE wall model produced inaccurate flow direction. Bae *et al.* (2018) recently showed that a new slip-velocity model is as accurate as the ODE equilibrium wall model in the same flow configuration.

It should be noted that this transient channel flow is equivalent to a shear-driven scenario where the walls accelerate in the spanwise direction with no body force applied on the flow (this is shown from the extended Galilean invariance property of the Navier-Stokes equation under uniform rectilinear accelerations). Therefore, three dimensionality diffused out slowly from the wall in viscous time scales. On the contrary, many 3DTBLs in engineering applications are pressure driven and spatially developing, where mean three dimensionality appears instantly in the outer layer through the inviscid vorticity tilting/skewing mechanism (Coleman, Kim & Spalart 1996, 2000). The streamwise variations of the spanwise pressure gradient, imposed by the wall geometry, often drives this process. Therefore, to better assess the performance of wall models for predicting 3DTBL, validation against spatially developing 3DTBLs at high Reynolds number is desired.

We report wall-modeled LES of a spatially developing 3DTBL in a bent square duct, following the experiment of Schwarz & Bradshaw (1994). We chose this case from the experimental investigations on 3DTBLs compiled in the review of Johnston & Flack (1996), based on the high Reynolds number of the flow considered and reasonable documentation of inflow and boundary conditions necessary in computational studies. We start by investigating the performance of an equilibrium wall model (Kawai & Larsson 2012), which a simple and widely used wall model.

This brief is organized as follows. The detailed methods of the present wall-modeled

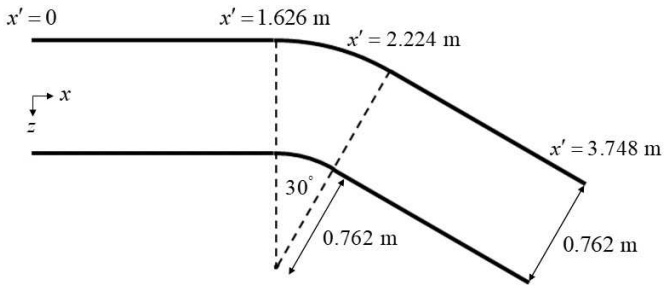

FIGURE 1. Flow configuration of the reference experiment of Schwarz & Bradshaw (1994). Here, the coordinate system (x, y, z) is aligned with the upstream section while the other coordinate system (x', y', z') is aligned with the local duct centerline.

LES are introduced in Section 2. Comparison between the present wall-modeled LES and experiment is presented in Section 3, followed by concluding remarks in Section 4.

2. Computational details

2.1. *Flow configuration*

Figure 1 shows the flow configuration of the reference experiment by Schwarz & Bradshaw (1994). It illustrates a bent square duct with a 0.762m × 0.762m cross-section and a streamwise length of 3.748 m. A spatially developing 3DTBL is generated by a 30° bend that imposes a cross-stream pressure gradient. The surface streamlines are deflected by up to 22° relative to the centerline velocity vector. Then, the created 3DTBL gradually recovers to a two-dimensional flow downstream of the bend. Following the experiment, two coordinate systems are defined in the present study (see Figure 1). The coordinate system (x, y, z) is aligned with the upstream section, where x, y, and z denote the streamwise, wall-normal, and spanwise directions, respectively. The other coordinate system (x', y', z') is aligned with the local duct centerline. (U, V, W) are corresponding mean velocity components for both coordinate systems.

2.2. *Flow solver and boundary conditions*

A wall-modeled LES is conducted using the code CharLES with a Voronoi mesh generator (Cascade Tech., Inc). The CharLES code solves the compressible Navier-Stokes equations with the static-coefficient Vreman model as the SGS model. The Voronoi mesh generator based on a hexagonal close packed (HCP) point-seeding method can automatically build high-quality meshes for arbitrarily complex geometries with minimal user inputs. First, a surface geometry of the square duct needs to be provided to describe the computational domain as shown in Figure 1. Second, the user must specify the coarsest grid resolution of the uniformly seeded HCP points. For the present wall-modeled LES, this length scale $\Delta s_{\max}$ is set to 0.01 m. The meshes are also refined in the near-wall region so that the number of grid cells across the local boundary layer thickness ranges from 8 to 11 along the streamwise direction. The resulting minimum cell size in the wall unit is $\Delta s^+_{\min} = \Delta s_{\min} u_\tau / \nu = 140$, and 30 million control volumes are used in total.

The wall-shear stress from the ODE equilibrium wall model (Kawai & Larsson 2012) is imposed as the wall boundary condition, and the wall is assumed to be isothermal.

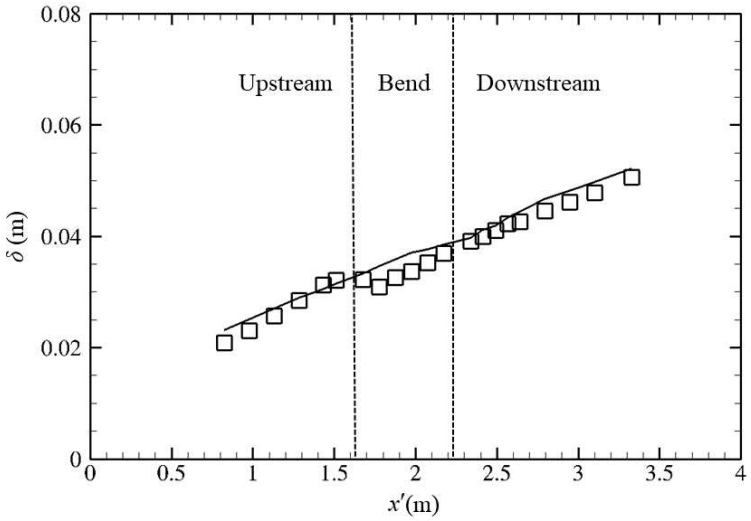

FIGURE 2. Boundary layer thickness distribution along the streamwise direction (x') measured at $z' = 0$. Vertical dashed lines indicate the bend start and end locations, respectively. Lines, present wall-modeled LES; squares, experiment (Schwarz & Bradshaw 1994).

At the matching location of the equilibrium wall model, temporally filtered LES data are provided to the wall model as suggested by Yang, Park & Moin (2017). The Navier-Stokes characteristic boundary condition for subsonic non-reflecting outflow is imposed at the outflow plane (Poinsot & Lele 1992). For the inflow boundary condition, a synthetic turbulence boundary condition is imposed to provide a realistic turbulent inflow condition that matches the experiment in the upstream section of the bend. To reproduce the upstream condition of the reference experiment, a series of separate simulations has been performed with different upstream section lengths. The computational domain is determined based on this numerical experiment, which starts at $x' = -0.813$ m (note that the flow configuration in Figure 1 starts at $x' = 0$ m) and ends at $x' = 3.748$ m (the same outlet location as the experiment). Consequently, the computational domain size of the present study is $(L_{x'} \times L_{y'} \times L_{z'}) = (4.561\text{ m} \times 0.762\text{ m} \times 0.762\text{ m})$. The Reynolds number based on the duct side length (0.762 m) and the inlet freestream velocity (26.5 m/s) is 1,400,000. The Reynolds number based on the local momentum thickness and the freestream velocity ranges from 4,000 to 9,000 ($Re_\tau = 1,200 - 2,400$).

3. Results and discussion

Figure 2 shows the boundary layer thickness distribution along the streamwise direction measured at $z' = 0$ (duct centerline). It should be noted that the flow is not fully developed, and the boundary layer thickness is a small fraction of the duct side length. Here, the boundary layer thickness (δ) is defined as the height at which the mean velocity magnitude reaches 99 percent of the freestream value. At $z' = 0$, the boundary layer grows along the top and bottom wall, and the averaged value of these two is represented. The

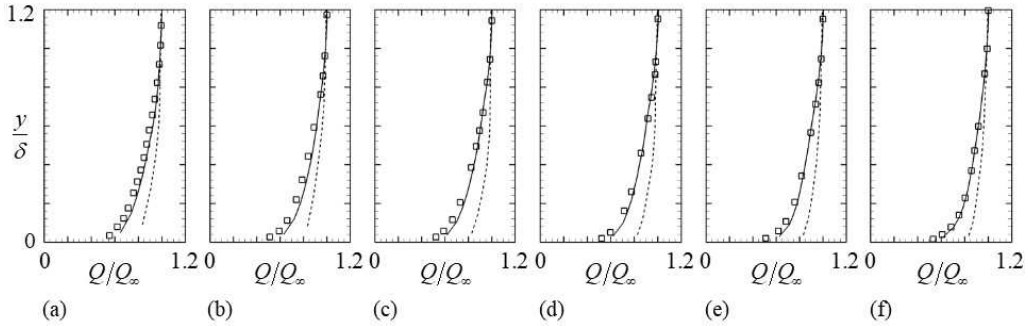

FIGURE 3. Normalized mean velocity profiles: (a) $x' = 0.978$ m; (b) $x' = 1.435$ m; (c) $x' = 1.775$ m; (d) $x' = 2.075$ m; (e) $x' = 2.415$ m; (f) $x' = 2.948$ m. Lines, present wall-modeled LES; squares, experiment (Schwarz & Bradshaw 1994); dashed lines, no-slip LES (without wall model).

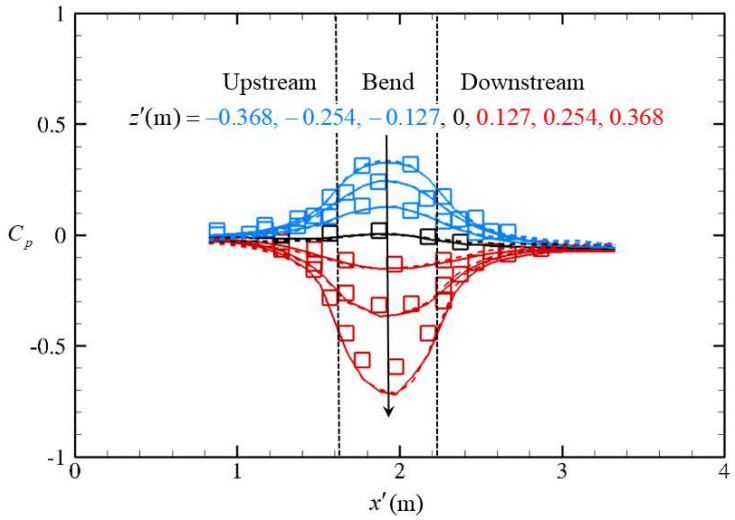

FIGURE 4. Mean pressure coefficient distribution along the streamwise direction (x') measured at $y' = 0$. Vertical dashed lines indicate the bend start and end locations, respectively. Lines, present wall-modeled LES; squares, experiment (Schwarz & Bradshaw 1994); dashed lines, no-slip LES (without wall model).

growth of the boundary layer thickness is in reasonable agreement with the experimental results, with the largest difference observed in the bend. In the bend section, the growth rate of δ in the experiment is slightly reduced while that of the wall-modeled LES is constantly increased. Figure 3 illustrates the mean velocity magnitude ($Q = \sqrt{U^2 + W^2}$) profiles normalized with the freestream value (Q_∞) as a function of the wall-normal distance. For comparison, the results of the no-slip LES (no wall model) using the same coarse mesh for the wall-modeled LES are also shown. Figures 3(a,b), (c,d), and (e,f)

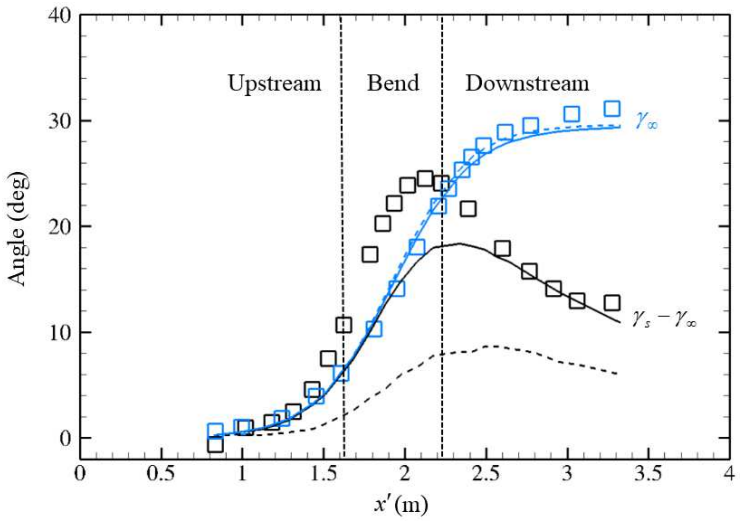

FIGURE 5. Surface crossflow angle relative to freestream ($\gamma_s - \gamma_\infty$) and freestream turning angle (γ_∞) distribution along the streamwise direction (x'). Vertical dashed lines indicate the bend start and end locations, respectively. Lines, present wall-modeled LES; squares, experiment (Schwarz & Bradshaw 1994); dashed lines, no-slip LES (without wall model).

correspond to the upstream section, bend, and downstream section, respectively. In the vicinity of the wall, there are some differences between the current wall-modeled LES and experiment, but overall, mean velocity profiles are predicted with reasonable accuracy. However, the discrepancy between the experiment and no-slip LES is much greater, showing that the equilibrium model provides some benefit.

Figure 4 illustrates an axial distribution of the mean pressure coefficient defined as $C_p = (P - P_{ref})/(\rho U_{ref}^2/2)$, where P is local pressure at given x', z', and $y' = 0$ (i.e. freestream wall-normal location); ρ is density; and P_{ref} and U_{ref} are the reference pressure and streamwise velocity at $x' = 0$, respectively. Various spanwise locations are considered. Along the concave wall ($z' < 0$), the value of C_p is positive, and along the convex wall ($z' > 0$) it becomes negative. Note that the results from both wall-modeled LES and no-slip LES are almost on top of each other at the freestream wall-normal location, because the inviscid mechanism dominates in the inviscid core region of the square duct. The differences between the current wall-modeled LES and experiment are observed within the bend, especially at the $z' > 0$ location, presumably because of the lack of the grid resolution across the thin boundary layer thickness distribution near the side wall. But these difference decreases as the 3DTBL inside the bend gradually recovers to the two-dimensional turbulent boundary layer in the downstream section.

Crossflow turning angles are defined as $\gamma = \tan^{-1} W/U$, where W and U are spanwise and streamwise mean velocity components with respect to the upstream coordinate (x, y, z). Their variations along the axial and wall-normal directions are represented in Figures 5 and 6, respectively. Here, γ_∞ is γ at the freestream, while γ_s is that at the surface. γ_∞ turns from 0° before the bend to 30° after the bend to accordance with the

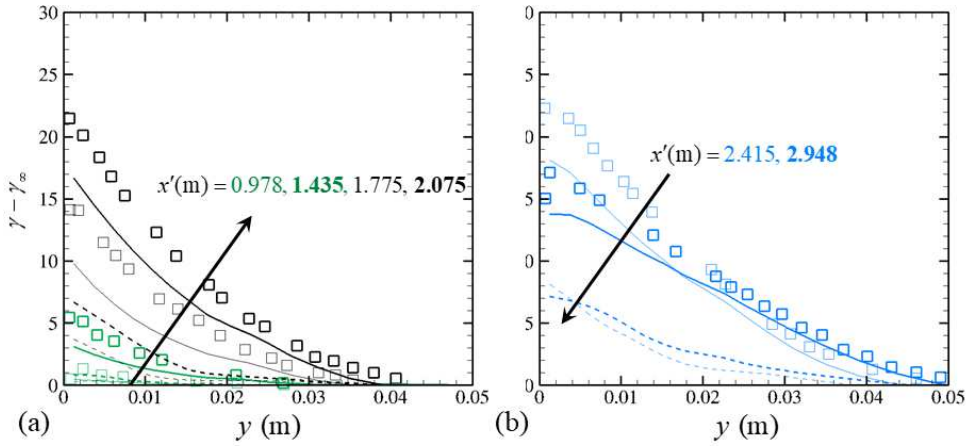

FIGURE 6. Crossflow angle relative to freestream: (a) crossflow development at $x'(\mathrm{m}) = 0.978, 1.435, 1.775, 2.075$; (b) crossflow decay at $x'(\mathrm{m}) = 2.415, 2.948$. Lines, present wall-modeled LES; squares, experiment (Schwarz & Bradshaw 1994); dashed lines, no-slip LES (without wall model).

specified geometry. Consistent with the mean pressure coefficient distribution, the flow turning angles at the freestream wall-normal location (γ_∞) from both the wall-modeled and no-slip calculations show excellent agreement with the experiment. The increase of the surface crossflow in the upstream and bend sections and its gradual decrease is captured from the current wall-modeled LES, but the magnitude of $\gamma_s - \gamma_\infty$ is underpredicted near the bend region. The maximum value of γ_s is larger than the 30° bend angle, and this shows the effect of the cross-stream pressure gradient generated by the bend on the surface streamline direction. Note that the current square duct flow is fully attached. Here, the wall-normal measurement location of the experiment for γ_s is $y^+ = 50$, which corresponds to the closest three-hole pressure probe measurement height. However, γ_s of the current wall-modeled LES is extracted at the first off-wall grid point ($y^+ = 70$). But this difference in wall-normal distance does not affect the current result since γ_s within the wall-modeled region is constant when the equilibrium wall model is utilized. Figure 6 indicates the profiles of crossflow angle relative to freestream with respect to the wall-normal direction. The crossflow angle increases until the end of the bend section (Figure 6(a)) and decays in the downstream section (Figure 6(b)). Figure 6 also shows that the current wall-modeled LES can predict this crossflow development and decay, although the predicted crossflow angles are smaller than the experiment. Consistent with Figure 5, the discrepancy between the current wall-modeled LES and experiment in $\gamma - \gamma_\infty$ increases with the cross-flow development and then decreases with its decay. Also, in figures 5 and 6, it is shown that the no-slip LES significantly underperforms the wall-modeled LES.

4. Conclusions

We conducted a wall-modeled LES of a spatially developing non-equilibrium turbulent boundary layer in a square duct with a 30° bend using a simple and widely used equilibrium wall model. We observed a fair prediction of mean velocity and pressure distribution

from the wall-modeled LES using a very coarse mesh. Discrepancy in the prediction of cross-flow angles was found largest in the bend region where departure from equilibrium is strongest, mainly caused by assumption of neglecting pressure gradient terms in the equilibrium wall model.

Future plans include a mesh adaptation/convergence studies to establish grid-independent wall-modeled LES results. Additionally, more advanced wall models including the partial differential equation/integral nonequilibrium wall models will be used to assess the wall-model performance. For this purpose, the legacy version of the CharLES code may complement the present study, as the new solver currently does not support other wall models.

One challenge in the present investigation is the uncertainty in the inlet boundary condition. It was not straightforward to reproduce the experimental condition in wall-modeled LES at the first measurement station upstream of the bend region, due to the missing details in the experiment close to the physical inlet of the test section. This mandated us to experiment with the length of the inlet development section where the velocity field develops realistic turbulent structures from artificial synthetic signals constructed from guessed mean and Reynolds stresses. To alleviate this issue, another experiment of a nonequilibrium 3DTBL over a bump swept at 45° by Webster, Degraaff & Eaton (1996) is currently under being considered as a companion investigation.

Acknowledgments

This investigation was funded by ONR Grant #N00014-16-S-BA10. MC is grateful to the scientists of Cascade Technologies, Inc. (in particular, Dr. Sanjeeb Bose) for their support on mesh generation and solver setup.

REFERENCES

Bae, H. J., Lozano-Durán, A., Bose, S. T. & Moin, P. 2018 Dynamic slip wall model for large-eddy simulation. *J. Fluid Mech.* **859**, 400–432.

Bose, S. T. & Park, G. I. 2018 Wall-modeled large-eddy simulation for complex turbulent flows. *Annu. Rev. Fluid Mech.* **5**, 535–561.

Chapman, D. R. 1979 Computational aerodynamics development and outlook. *AIAA J.* **17**, 1293–1313.

Choi, H. & Moin, P. 2012 Grid-point requirements for large eddy simulation: Chapman's estimates revisited. *Phys. Fluids* **24**, 011702.

Coleman, G. N., Kim, J. & Spalart, P. R. 1996 Direct numerical simulation of strained three-dimensional wall-bounded flows. *AIAA Paper* **96-0655**, 1–8.

Coleman, G. N., Kim, J. & Spalart, P. R. 2000 A numerical study of strained three-dimensional wall-bounded turbulence. *J. Fluid Mech.* **416**, 75–116.

Deardorff, J. W. 1970 A numerical study of three-dimensional turbulent channel flow at large Reynolds numbers. *J. Fluid Mech.* **41**, 453–480.

Giometto, M. G., Lozano-Durán, A., Park, G. I. & Moin, P. 2017 Three-dimensional transient channel flow at moderate Reynolds numbers: Analysis and wall modeling. *Annual Research Briefs*, Center for Turbulence Research, Stanford University, pp. 193-205.

Jiménez, J. & Moser, R. D. 2000 Large-eddy simulations: where are we and what can we expect?. *AIAA J.* **38**, 605–612.

Johnston, J. P. & Flack, K. A. 1996 Review–advances in three-dimensional turbulent boundary layers with emphasis on the wall-layer regions. *J. Fluids Eng.* **118**, 219–232.

Kawai, S. & Larsson, J. 2012 Wall-modeling in large eddy simulation: length scales, grid resolution, and accuracy. *Phys. Fluids* **24**, 015015.

Larsson, J., Kawai, S., Bodart, J. & Bermejo-Moreno, I. 2016 Large eddy simulation with modeled wall-stress: recent progress and future directions. *Mech. Eng. Rev.* **3**, 15-00418.

Park, G. I. & Moin, P. 2014 An improved dynamic non-equilibrium wall-model for large eddy simulation. *Phys. Fluids* **26**, 015108.

Piomelli, U. 2008 Wall-layer models for large-eddy simulations. *Porg. Aerosp. Sci.* **44**, 437–446.

Poinsot, T. & Lele, S. K. 1992 Boundary conditions for direct simulation of compressible viscous flows. *J. Comput. Phys.* **101**, 104–129.

Sayadi, T. & Moin, P. 2012 Large eddy simulation of controlled transition to turbulence. *Phys. Fluids* **24**, 114103.

Schumann, U. 1975 Subgrid scale model for finite difference simulations of turbulent flows in plane channels and annuli. *J. Comput. Phys.* **18**, 376–404.

Schwarz, W. R. & Bradshaw, P. 1994 Turbulence structural changes for a three-dimensional turbulent boundary layer in a 30° bend. *J. Fluid Mech.* **272**, 183–209.

Slotnick, J., Khodadoust, A., Alonso, J., Darmofal, D., Gropp, W., Lurie, E. & Mavriplis, D. 2014 CFD Vision 2030 Study: A Path to Revolutionary Computational Aerosciences. *NASA/CR-2014-218178*, 1–51.

Spalart, P. R. 2009 Detached-eddy simulation. *J. Fluid Mech.* **205**, 319–340.

Webster, D. R., Degraaff, D. B. & Eaton, J. K. 1996 Turbulence characteristics of a boundary layer over a swept bump. *J. Fluid Mech.* **323**, 1–22.

Yang, X. I. A., Sadique, J., Mittal, R. & Meneveau, C. 2015 Integral wall model for large eddy simulations of wall-bounded turbulent flows. *Phys. Fluids* **27**, 025112.

Yang, X. I. A., Park, G. I. & Moin, P. 2017 Log-layer mismatch and modeling of the fluctuating wall stress in wall-modeled large-eddy simulations. *Phys. Rev. Fluids* **2**, 104601.